Quantifying the Excitonic Static Disorder in Organic Semiconductors

Austin M. Kay, Oskar J. Sandberg,* Nasim Zarrabi, Wei Li, Stefan Zeiske, Christina Kaiser, Paul Meredith, and Ardalan Armin*

Organic semiconductors are disordered molecular solids, and as a result, their internal charge generation dynamics, charge transport dynamics, and ultimately, the performance of the optoelectronic devices they constitute, are governed by energetic disorder. This is particularly pertinent for emerging photovoltaic technology where the extractable power is directly dependent on these dynamics. To ascertain how energetic disorder impacts charge generation, exciton transport, charge transport, and the performance of organic semiconductor devices, an accurate approach is first required to measure this critical parameter. In this work, it is shown that the static disorder of an organic semiconductor can be obtained from its photovoltaic external quantum efficiency spectrum at wavelengths near the absorption onset. A detailed methodology is presented, alongside a computational framework, for quantifying the static energetic disorder associated with singlet excitons. Moreover, the authors show that minimizing the limiting effects of optical interference is crucial for achieving high-accuracy quantifications. Finally, transparent devices are employed to estimate the excitonic static disorder in several technologically relevant organic semiconductor donor–acceptor blends, including the high-efficiency organic photovoltaic system PM6:Y6.

1. Introduction

Organic semiconductors combine the electronic advantages of semiconducting materials, including the ability to conduct electricity and absorb or emit light, with the chemical and mechanical benefits of organic compounds such as flexibility, ease of processing, a very large palette of possible chemical combinations, and tailorable optical properties.[1–3] Such properties make organic semiconductors suitable for several applications, including organic light-emitting diodes (OLEDs)—a key component of the thin-film display technology utilized in smartphones and low power consumption televisions. Other avenues-of-research that have recently attracted considerable attention include the use of organic semiconductors in photovoltaic applications such as organic solar cells and indoor photovoltaics.[3–8] The efficiency at which organic solar cells convert solar energy into electrical power, the power conversion efficiency (PCE), has seen a steady increase over the past few years with 18% now in hand and the milestone of 20% expected to be reached imminently.[3,9,10] Currently, these cells suffer from a number of limitations including insufficient light-harvesting, short exciton diffusion lengths (important as organic semiconductors are excitonic at room temperature), large non-radiative recombination losses, and low charge carrier mobilities.[11] Provided that these limitations can be overcome, organic solar cells are anticipated to eventually reach a maximum PCE of approximately 25%.[3] Compared with lead-halide perovskite solar cells with PCEs greater than 25% (and indeed more conventional materials with similar unique selling points such as copper indium selenide), it is clear that further investigations must be conducted to push the PCE of organic solar cells to its predicted theoretical boundary, nudging them towards commercial visibility.[12–14]

One of the first-order limiting factors on the PCE of an organic solar cell is the static energetic disorder (or, more simply, the "static disorder") of the active organic semiconductor layer; an inherent characteristic of molecular solids. The static disorder is defined by the broadness of the density of states (DOS) of species within the active layer and is commonly approximated by either a Gaussian or exponential distribution.[15] An increased static disorder generally correlates with an increased number of trap-like states in the gap and is typically associated with a degraded transport of excitations and charges through the active layer.[16–21] Nevertheless, the role of static disorder in organic solar cells has remained controversial. Increased levels of energetic disorder have been shown to be detrimental to organic solar cell performance, resulting in reduced fill factors, short circuit current densities, and open-circuit voltages (V_{OC}).[19,22–24] Conversely, it has been suggested that higher levels of static disorder near the donor–acceptor (D:A – the *n*-and-*p*-type components making up the photo-junction, respectively) interface facilitate charge separation, thus enhancing charge generation

A. M. Kay, O. J. Sandberg, N. Zarrabi, W. Li, S. Zeiske, C. Kaiser, P. Meredith, A. Armin
Sustainable Advanced Materials (Sêr-SAM)
Department of Physics
Swansea University
Singleton Park, Swansea SA2 8PP, United Kingdom
E-mail: o.j.sandberg@swansea.ac.uk; ardalan.armin@swansea.ac.uk

and reducing recombination.[25] Therefore, while a low disorder for free charges across the bulk is desired to ensure efficient transport, an increased level of energetic disorder associated with charge-transfer (CT) states at the D:A interface might be beneficial for the charge generation-recombination dynamics.[26]

With the emergence of so-called low-offset D:A systems based on non-fullerene acceptors, the role of exciton dynamics has become increasingly important, defining the radiative PCE limit in state-of-the-art organic solar cells.[27–31] However, the effect of the excitonic disorder on the charge-recombination dynamics has remained poorly understood. Furthermore, the disorder associated with excitons is generally different from the disorder associated with free charge carriers, which is believed to reflect the energetic distribution of the corresponding molecular orbital energies. By quantifying, understanding, and minimizing the (potentially) adverse effects of the excitonic disorder, the device performance could be optimized in organic solar cells, bringing the PCE closer to its theoretical limit. To this end, a reliable approach is therefore required to quantify the excitonic static disorder.

Energetic disorder in organic semiconductors is typically quantified using one of a few different methodologies. These include Kelvin probe and temperature-dependent charge carrier mobility measurements to probe the disorder of charges, and temperature-dependent photovoltaic external quantum efficiency (EQE_{PV}) measurements to estimate the static disorder of CT states.[32–36] A method for quantifying the energetic disorder of excitons, based on wavelength-dependent internal quantum efficiency measurements in neat organic semiconductors, was recently proposed by Hood et al..[37] While this method has several benefits, including single-temperature measurements, the technique cannot be adapted from neat organic semiconductors to D:A blends. In blends, the excitonic disorder has been inferred from the Urbach energy extracted from the sub-gap absorption tail, assuming an exponential shape and distribution.[22,26,38] However, the spectral range is often limited by the absorption of CT states and mid-gap trap states.[39,40] Furthermore, Kaiser et al. recently found that the apparent Urbach energy in several technologically-relevant blend systems is strongly photon energy-dependent, consistent with a Gaussian DOS rather than an exponential DOS, and saturates to the thermal energy at low enough photon energies.[31] Finally, as it is challenging to directly measure the sub-gap absorption coefficient, it is commonly inferred from the EQE_{PV}. However, it has been shown that the line-shape of the EQE_{PV} is affected by optical interference.[41,42] Optical interference effects, or optical cavity effects, arise from internal reflection and refraction inside the device stack of thin-film cells; such effects result in strongly wavelength-dependent absorption profiles, adding an additional photon energy dependence to EQE_{PV}.

In this work, we propose a methodology (along with a computational framework) for quantifying the static energetic disorder associated with excitons from EQE_{PV} spectra, allowing for the excitonic static disorder of several systems to be estimated. For improved accuracy, we show that the optical cavity effects that arise inside thin-film photovoltaics must be minimized. To this end, we propose the use of two transparent device architectures. The first architecture is a thin-film photovoltaic device with a photoresistor-like architecture, the "lateral structure", that offers minimal optical interference at the expense of poor charge

collection. The second architecture is that of an organic solar cell with a transparent top electrode that results in far less internal reflection (compared with the conventional organic solar cell architecture, which has one reflecting metallic electrode). Using these "minimal-interference devices", we have quantified the excitonic static disorder in five organic semiconductor D:A blends, including the high efficiency (current "fruit fly") PM6:Y6 system (see Experimental Section for chemical definitions).

2. Results and Discussion

2.1. Methodology for Quantifying Excitonic Disorder from Sub-Gap Absorption

To begin the analysis, we quantified the static energetic disorder associated with excitons, σ_S, by applying a model for the sub-gap singlet exciton (SE) absorption coefficient (α) to the spectral regime characterized by SE absorption. In D:A blends, α is characterized by excitons in the component with the narrower gap; hence, the relevant optical gap (E_{opt}) can be expressed as $E_{opt} = \min(E_D, E_A)$, where E_D and E_A are the SE energies of the donor and acceptor, respectively. As a consequence, the methodology can only be used to characterize the narrower optical gap component of a D:A blend. In the model, we assume the sub-gap absorption coefficient to be of the form $\alpha(E) = \int_0^\infty \alpha_0(E'_{SE}, E) g_{DOS}(E'_{SE}) dE'_{SE}$, where $\alpha_0(E'_{SE})$ is the absorption coefficient of a singlet exciton mode at energy E'_{SE}, while g_{DOS} describes the excitonic density of states. In the case of a Gaussian distribution, this DOS is centered around the mean optical gap (E_{opt}), has a standard deviation σ_S that quantifies the excitonic static disorder, and is given by

$$g_{DOS}\left(E'_{SE}\right) = \frac{N_{SE}}{\sqrt{2\pi\sigma_S^2}} \exp\left(-\frac{\left[E'_{SE} - E_{opt}\right]^2}{2\sigma_S^2}\right) \tag{1}$$

where N_{SE} is the number density of excitonic states in the active layer.

The absorption of CT states of a single energy mode has generally been described as a Marcus charge-transfer process or with related extensions including molecular vibrations.[39,43,44] For excitons, however, Kaiser et al. recently suggested that sub-gap SE absorption is better described by a Boltzmann factor.[31] In that framework, the resulting absorption coefficient of an SE mode of energy E'_{SE}, at an incident photon energy E, can be approximated as

$$\alpha_0\left(E, E'_{SE}\right) \approx \alpha_{sat} \begin{cases} 1, & \text{for } E \geq E'_{SE}, \\ \exp\left[-\dfrac{E'_{SE} - E}{k_B T}\right], & \text{for } E < E'_{SE} \end{cases} \tag{2}$$

where k_B is the Boltzmann constant, T is the temperature, and α_{sat} is a pre-factor that holds a weak photon energy-dependence. Such dependence can also be justified in terms of a generalized non-adiabatic Marcus theory, assuming the electronic transfer to be between a localized ground state and a diffuse excited state (in the weak-coupling limit).[31,45–47] The associated sub-gap

absorption coefficient, determined by integrating the product of Equation (1) and (2) with respect to E'_{SE}, is obtained as

$$\alpha(E) = \frac{\alpha_{sat}}{2}\left\{\exp\left[\frac{E - E_{opt} + \frac{\sigma_S^2}{2k_BT}}{k_BT}\right]\text{erfc}\left[\frac{E - E_{opt} + \frac{\sigma_S^2}{k_BT}}{\sigma_S\sqrt{2}}\right] + 1 + \text{erf}\left[\frac{E - E_{opt}}{\sigma_S\sqrt{2}}\right]\right\}$$

(3)

where erf denotes the error function and erfc denotes the complementary error function.[31]

In practice, it is challenging to directly measure the sub-gap absorption coefficient of an optoelectronic device.[41] Instead, in this work, we inferred the sub-gap absorption coefficient from sensitive EQE_{PV} measurements, which are superior in sensitivity to other methods such as Fourier transform photocurrent and photothermal deflection spectroscopy.[48] In the case of weakly-absorbing sub-gap features, characterized by $\alpha(E)d_{AL} \ll 1$ (where d_{AL} is the active layer thickness), it is usually assumed that $EQE_{PV}(E) \propto \alpha(E)d_{AL}$. However, this condition may fail for sub-gap excitons near the optical gap and therefore, to account for absorption in the active layer, we write

$$EQE_{PV}(E) = EQE_0\left[1 - e^{-\alpha(E)d_{AL}}\right]$$

(4)

where EQE_0 is a pre-factor that, in general, holds a photon energy dependence.[42] However, in the following we approximate EQE_0 to be constant within the spectral range of interest, corresponding to a uniform net intensity transmission into the active layer, minimal back-reflection, and a wavelength-independent internal quantum efficiency in the device.[49] The validity of this underpinning approximation is explored at length for three device architectures in Section S2.3 (Supporting Information). In the limit that this assumption holds, the static disorder can be quantified by applying Equations (3) and (4) to the spectral regime characterized only by singlet exciton absorption.

To precisely identify the excitonic sub-gap regime and to avoid other, more subtle absorption features present in organic semiconductors, including trap state and CT state characteristics, we utilize the (photon energy-dependent) apparent Urbach energy (E_U^{app}) given by[31]

$$E_U^{app}(E) = \left[\frac{d\ln\left[EQE_{PV}(\varepsilon)\right]}{d\varepsilon}\Bigg|_{\varepsilon = E}\right]^{-1}$$

(5)

Through Equation (5), the subtle absorption characteristics of CT states and trap states result in prominent features in the apparent Urbach energy and therefore, the spectral regime corresponding to SE absorption is identified more easily. **Figure 1a** shows sub-gap absorption tails obtained using Equation (3) and (4), assuming $E_{opt} = 1.60$ eV and $k_BT = 25.3$ meV, for σ_S varied from 20 to 100 meV. Based on Equation (3), in the case of sub-gap SE absorption, two distinct regimes can be identified.
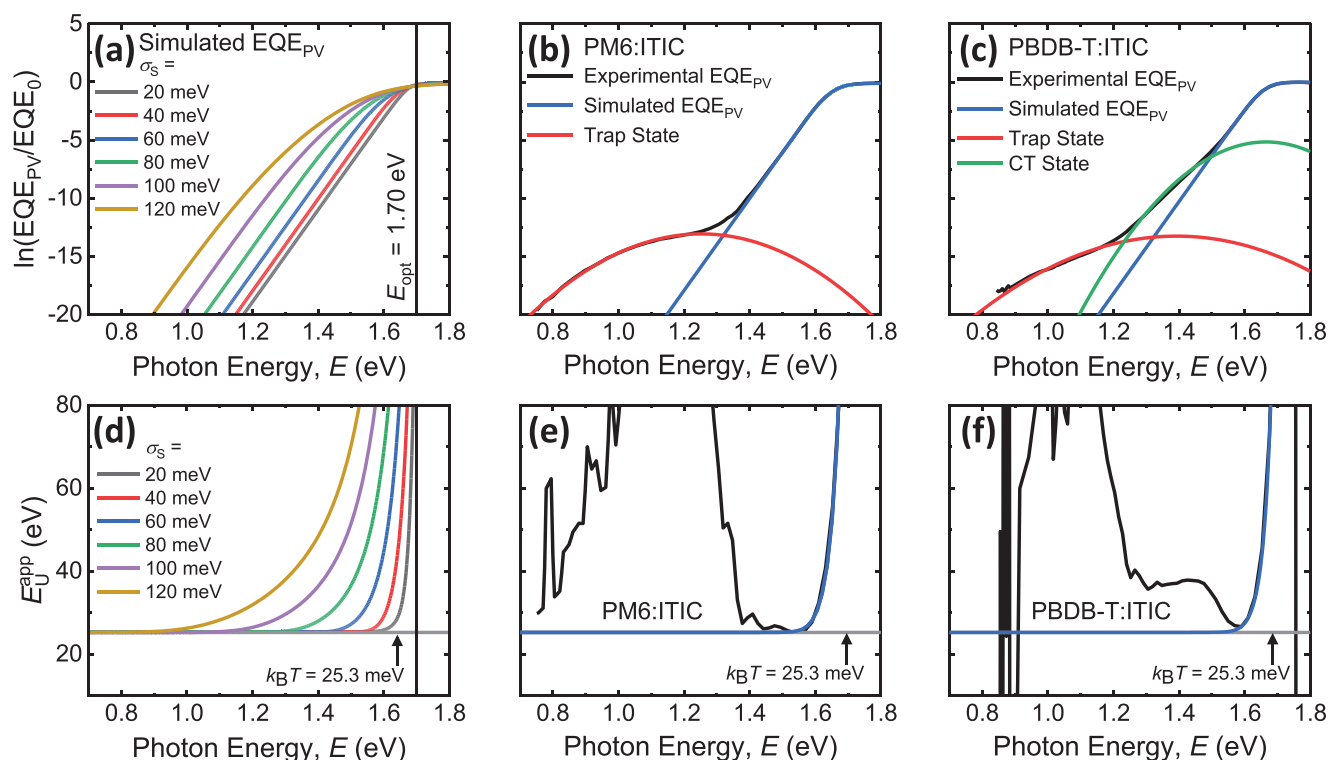

Figure 1. A comparison between theoretical and experimental EQE_{PV} spectra and the corresponding apparent Urbach energy spectra. a) The natural logarithm of sub-gap EQE_{PV} tails characterized by singlet exciton absorption, created using Equation (3) and (4), with $E_{opt} = 1.60$ eV, $k_BT = 25.3$ meV, and σ_S varied from 20 to 120 meV. b) and c) show the sensitive EQE_{PV} spectra of PM6:ITIC and PBDB-T:ITIC bulk heterojunctions, respectively. The Gaussian absorption features of trap states and CT states are indicated by the red and green lines, respectively. The apparent Urbach energy spectra shown in d–f were determined from a–c using Equation (5). Note that all chemical definitions are provided in Experimental Section and that the data used to generate all main text and supporting figures can be found in the "Supporting Data" Excel file in the Supporting Information.

ADVANCED
SCIENCE NEWS
www.advancedsciencenews.com

ADVANCED
FUNCTIONAL
MATERIALS
www.afm-journal.de

As shown in Figure 1a, at photon energies far below the optical gap $\left(E < E_{\text{opt}} - \frac{\sigma_S^2}{k_B T}\right)$, $\alpha(E)$ grows exponentially with increasing photon energy. This region of exponential growth results in $E_U^{\text{app}}(E) \to k_B T$, a constant, regardless of the magnitude of the excitonic static disorder, as shown by the coalescence of the simulated apparent Urbach energy spectra with the grey line in Figure 1d. In turn, at higher photon energies (where $E \to E_{\text{opt}}$ and $\alpha(E) \to \alpha_{\text{sat}}$), the sub-gap absorption eventually takes a Gaussian-like shape as the apparent Urbach energy becomes strongly dependent on the photon energy E, ultimately increasing by orders of magnitude as $\frac{\partial \alpha(E)}{\partial E} \to 0$.

To demonstrate the applicability of our model, we apply it to the experimentally-determined EQE_{PV} spectra of PM6:ITIC and PBDB-T:ITIC bulk-heterojunctions (BHJs – where the photoactive layer is a molecular blend of D and A) with inverted device architectures, as shown in Figure 1b,c. The corresponding apparent Urbach energy spectra are shown in Figure 1e,f. Using these spectra, the appropriate spectral regimes characterized by the behavior of SEs were identified. The lower limit of the SE-dominated spectral regime was defined as the point where deviations due to the Gaussian absorption features of trap states (and CT states in higher-offset systems like PBDB-T:ITIC) become apparent.[39,40] In Figure 1, these additional absorption features (which are not relevant to the quantification of the excitonic static disorder) are indicated by the red and green lines for trap states and CT states, respectively. The parametrization of these absorption features is described in Section S1 (Supporting Information). On the other hand, the upper limit of the SE-dominated spectral regime was defined as the "first saturation peak", i.e., the first maximum that follows the sub-gap tail, corresponding to $\alpha(E) \approx \alpha_{\text{sat}}$. After identifying the upper and lower limits using the above criteria, Equation (3) and (4) were applied to the appropriate regimes of Figure 1c,d, with values for parameters-of-interest being extracted and used to simulate the SE-characterized EQE_{PV} and E_U^{app} spectra shown by the blue lines. From Figure 1, it is evident that, when a Gaussian DOS is assumed, the excitonic sub-gap behavior

can be described well by Equation (3). It should be noted that this behavior cannot be reproduced if an exponential DOS and/or Marcus charge-transfer is instead assumed in Equation (1) and Equation (2), respectively, as neither reproduces the $k_B T$-dependent exponential tail that is observed.[31]

The methodology for accurately quantifying the excitonic static disorder is summarized in three steps: First, the EQE_{PV} spectrum must be normalized with respect to its value at the first saturation peak, EQE_{FSP}, where it is assumed that $\alpha(E) \approx \alpha_{\text{sat}}$ and thus, the normalized spectra should eventually be fit with Equation (4) divided by $EQE_{\text{FSP}} \approx EQE_0[1 - \exp(-\alpha_{\text{sat}} d_{\text{AL}})]$. In the limit that EQE_0 is spectrally-flat across the region of SE-absorption, then this degree of freedom can be removed through normalization (we found this produced a higher accuracy in the remaining degrees of freedom: α_{sat}, E_{opt}, and σ_S). The second step of the methodology is to identify the lower limit of the suitable spectral regime using the apparent Urbach energy. This lower limit is specified as the point where the line-shape ceases to be SE-characterized, whether that be due to the effects of CT states, trap states, or optical interference. Finally, Equation (3) and (4) must not be applied to EQE_{PV} at $E > E_{\text{opt}}$, i.e., after the first saturation peak is reached (and $\alpha(E) \approx \alpha_{\text{sat}}$). This must be avoided due to the weak energy-dependence of the pre-factor, α_{sat}, playing a more pivotal role. All these steps were followed when using the SE absorption model as neglecting them would likely result in an inaccurate quantification of the excitonic static disorder.

2.2. Experimental Results Without Cavity Correction

With the methodology for quantifying energetic disorder established, it was applied to the experimentally-determined EQE_{PV} spectra of several systems to quantify their excitonic static disorder. The EQE_{PV} spectra measured for PM6:Y6 BHJs of varying active layer thicknesses, d_{AL}, are shown in **Figure 2**a. In addition, the values for the excitonic static disorder and the optical gap, extracted by fitting these curves with Equation (3) and (4), are plotted in Figure 2b.
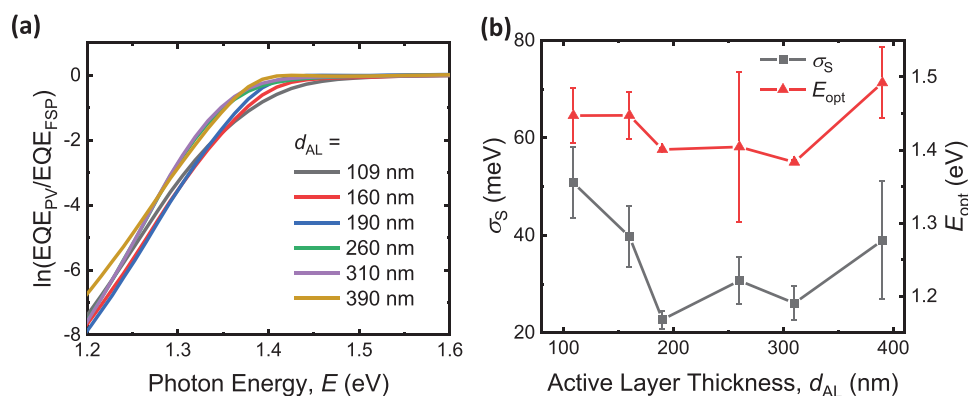

Figure 2. The apparent active layer thickness-dependence of the excitonic static disorder values extracted from EQE_{PV} measurements for PM6:Y6 BHJs with an inverted device architecture. In this blend, the narrower optical gap component, for which the characteristic excitonic static disorder and optical gap were determined, was Y6. a) The natural logarithm of normalized EQE_{PV} spectra measured for PM6:Y6 BHJs of varying active layer thickness at room temperature. These spectra were normalized with respect to EQE_{PV} at the first saturation peak, EQE_{FSP}. b) The values for the excitonic static disorder (σ_S) and the optical gap (E_{opt}) extracted through the application of Equation (3) and (4) to the normalized EQE_{PV} spectra of a). The error bars represent the statistical uncertainty in the extracted values obtained through the fittings.

As shown in Figure 2b, an apparent active layer thickness-dependence can be seen in the excitonic disorder values extracted for PM6:Y6 BHJs. Note that, for PM6:Y6, the narrower optical gap component was Y6, and the extracted σ_S and E_{opt} values therefore characterize this component. A corresponding thickness dependence was also observed in several other systems, including PBDB-T:ITIC, PM6:BTP-eC9, and PM6:ITIC systems (see Figure S1, Supporting Information). Although slight variations could be expected in the static disorder values extracted for two BHJs of a given blend of differing active layer thickness (e.g., due to thickness-dependent variations in the device fabrication), it is unlikely that the excitonic static disorder would vary to the extent it appears to in Figure 2b. As we investigate at length (using detailed optical simulations) in the next section, we believe that these thickness-dependent variations in the extracted static disorder values stem from subtle fluctuations in the line shapes of the EQE_{PV} spectra. Such variations can be attributed to the optical cavity effects that arise inside thin-film photovoltaic cavities like BHJs.

2.3. Investigating Optical Cavity Effects Through Simulation

To demonstrate the limitations imposed on the methodology by optical cavity effects, we now summarize an investigation in which EQE_{PV} spectra were simulated using an optical transfer-matrix model.[50] In this model, excitons are generated in the active layer of a multi-layered structure through the absorption of photons from an optical electric field distribution. This distribution is determined by accounting for the transmission and reflection of light at each interface using the refractive index, $\eta(E)$, and extinction coefficient, $\kappa(E)$, of all layers; for the optical constants of all layers bar the active layer, see Figure S2 (Supporting Information). To model the active layer, realistic $\eta(E)$ and $\kappa(E)$ were used, with the assumption that the sub-gap extinction coefficient depends on σ_S in accordance with Equation (3), noting that $\kappa(E) = \hbar c\alpha(E)/2E$, where $\hbar$ is the reduced Planck constant and c is the speed of light in vacuum.[50] The corresponding $\eta(E)$ and $\kappa(E)$ are shown in **Figure 3** for the case of low disorder ($\sigma_S = 40$ meV) and high disorder ($\sigma_S = 100$ meV), assuming $\alpha_{sat} = 0.0113$ nm^{-1}, $E_{opt} = 1.55$ eV, and $k_B T = 25.3$ meV for the sub-gap $\kappa(E)$ tails.

To explore and overcome the effects of optical interference, the methodology for quantifying the excitonic static disorder was applied to the simulated EQE_{PV} spectra of devices of three different device architectures. The first architecture, shown in **Figure 4**a, is that of an inverted organic solar cell with a highly-reflective top electrode (silver, Ag). In this figure, "ITO" and "ZnO" stand for the transparent conductor indium tin oxide and the electron transport layer zinc oxide, respectively. Furthermore "MoO$_3$" denotes the hole transport layer molybdenum trioxide. The second architecture, shown in Figure 4b, is very similar to the first but instead of a highly-reflective top electrode, it possesses a transparent one (indium zinc oxide, abbreviated to "IZO") that produces far less internal reflection and consequently, results in reduced optical interference in the active layer. Finally, the third architecture that was investigated (shown in Figure 4c) was an active layer film deposited onto a glass substrate—this architecture is herein referred
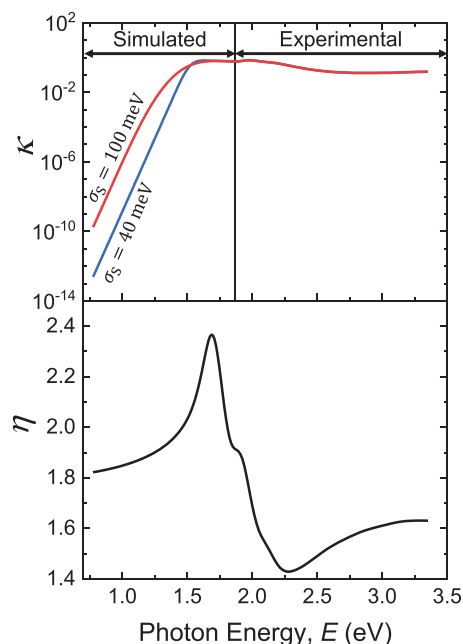

Figure 3. The optical constants used to describe the active layer in the optical transfer-matrix model. The sub-gap extinction tails were adapted from sub-gap absorption tails created using Equation (3), with $\alpha_{sat} = 0.0113$ nm^{-1}, $E_{opt} = 1.55$ eV, $k_B T = 25.3$ meV, and either $\sigma_S = 40$ meV or $\sigma_S = 100$ meV, then appended to the experimental above-gap data. The refractive index values were wholly experimental and describe a PM6:ITIC active layer.

to as the "lateral structure". Alongside the minimal number of interfaces the lateral structures possess, the use of small metallic electrodes at opposite ends of the device minimizes the amount of back-reflection, culminating in negligible optical interference inside the active layer.

Using the optical transfer-matrix model, the EQE_{PV} spectra shown in Figure 4d–i were simulated for all three device architectures using both sub-gap tails shown in Figure 3. In each case, the internal quantum efficiency for photon conversion was assumed to be spectrally-flat (and equal to unity for simplicity) and the effect of the incoherent glass layer at the front of each device was taken into account.[51,52] For each device architecture, the thickness of the active layer (d_{AL}) was varied from 50 nm to 350 nm to explore any potential d_{AL}-dependencies in the extracted static disorder values. Comparing Figure 4d with Figure 4e,f, the effect of optical interference on the line shapes of the EQE_{PV} spectra for organic solar cells with a reflective top electrode are immediately apparent; The sub-gap tails are quite disorganized compared with those of the lateral structure's EQE_{PV} spectra. There is some uniformity across the sub-gap tails for the organic solar cells with transparent top electrodes, but not to the extent that is observed for the lateral structures. The same conclusion can be drawn from the EQE_{PV} spectra simulated using $\sigma_S = 100$ meV, shown in Figure 4g–i.

To optimize the upper and lower limits of fittings to EQE_{PV} spectra (with the aim of accurately estimating the excitonic static disorder), a MATLAB script (provided in the Supporting Information) was developed to automate the fitting process. The script applies Equation (3) and (4) to the appropriate spectral regime
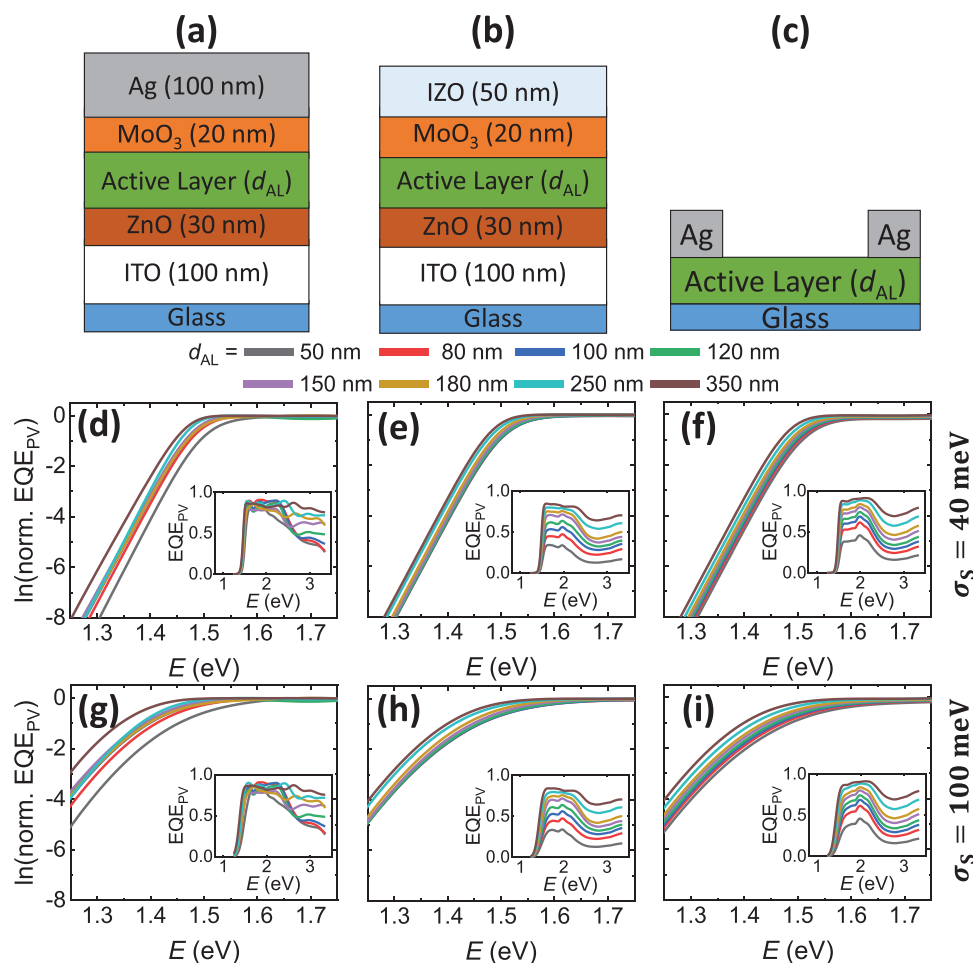
ADVANCED
SCIENCE NEWS
www.advancedsciencenews.com

ADVANCED
FUNCTIONAL
MATERIALS
www.afm-journal.de

Figure 4. Simulating EQE_{PV} spectra for devices of varying active layer thickness, for three architectures. a–c) The three device architectures considered in these simulations: organic solar cells with a) reflective top electrodes and b) transparent top electrodes, and c) lateral structures. The natural logarithm of the normalized EQE_{PV} spectra, simulated for devices of each architecture with a variety of active layer thickness (from 50 to 350 nm), are shown for the $\sigma_S = 40$ meV case in d–f) and for the $\sigma_S = 100$ meV case in g–i).

of an input EQE_{PV} spectrum, determines the optimal upper and lower limits, and outputs values for the parameters-of-interest. For each of the EQE_{PV} spectra shown in Figure 4d–i, the MATLAB script was used to determine the associated excitonic static disorder—the extracted values from all spectra are plotted as a function of active layer thickness in **Figure 5**. From this figure, it is clear that values extracted for the organic solar cells with a reflective top electrode fluctuate far more with increasing active layer thickness than the values extracted for both the organic solar cells with a transparent top electrode and the lateral structures.

Three conclusions can be drawn from the results shown in Figure 5: First, the variations are the result of optical cavity effects. This is demonstrated by, for example, the large absolute error in the excitonic disorder values obtained using organic solar cells with a reflective top electrode. As discussed in Section S2.3 (Supporting Information), this error is a result of variations in the pre-factor EQE_0 with changing photon energy, leading to a larger degree of warping of the sub-gap tails and, as a result, a more inaccurate quantification of the disorder.[42] Secondly, from an optical interference point-of-view, the excitonic disorder is most accurately quantified in devices with a

lateral structure, as shown by the close correlation between the input values ($\sigma_S = 40$ meV and $\sigma_S = 100$ meV) and the extracted values. From this perspective, the second-most accurate quantification of the static disorder is obtained using organic solar cells with a transparent top electrode. There are, however, subtle oscillations with increasing active layer thickness. Nevertheless, for devices with this architecture and $d_{AL} < 250$ nm, all extracted values are within approximately $\pm 10\%$ of the simulation input values. Whereas the least-accurate quantification of the static disorder is obtained for the organic solar cells with highly-reflective metallic electrodes, indicating their impracticality for this application. The third conclusion we draw from Figure 5 is that the excitonic static disorder is most likely to be accurately quantified using organic cells with transparent top electrodes, noting that from an experimental/practical point of view, they have a more optimized architecture (compared to lateral structures). Based on these conclusions, all values for the excitonic static disorder that were extracted from experimentally-determined EQE_{PV} spectra (for lateral structures and for cells with transparent top electrodes and active layer thicknesses less than 250 nm) were attributed a $\pm 10\%$ relative uncertainty.
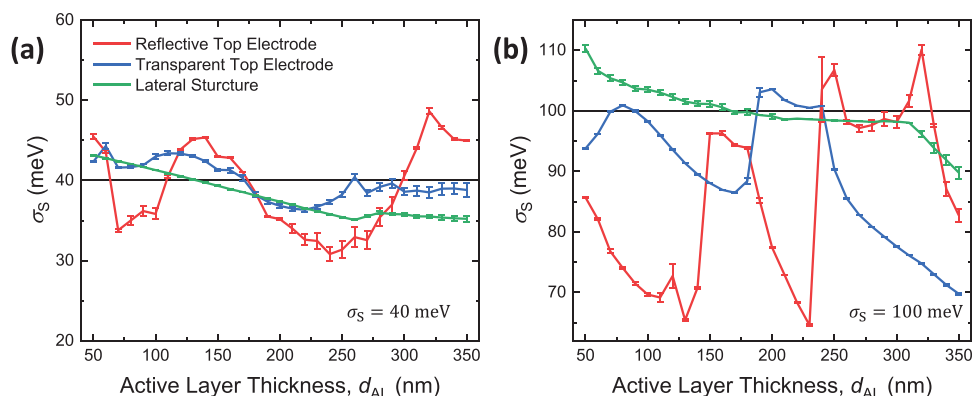
**ADVANCED
SCIENCE NEWS**

www.advancedsciencenews.com

**ADVANCED
FUNCTIONAL
MATERIALS**

www.afm-journal.de

Figure 5. The excitonic static disorder values extracted from the simulated EQE$_{PV}$ spectra shown in Figure 4d–i using the MATLAB script provided in the Supporting Information, for the three architectures illustrated in Figure 4a–c with active layers described by both a) $\sigma_S = 40$ meV and b) $\sigma_S = 100$ meV.

2.4. Experimental Results with Cavity Correction

To demonstrate how the line-shapes of the EQE$_{PV}$ spectra of transparent devices are less affected by optical interference, a comparison is made between two PTB7-Th:PC$_{71}$BM devices of comparable active layer thickness in **Figure 6**a, with one possessing a (conventional) reflective top electrode architecture and the other being a lateral structure. Furthermore, to demonstrate the utility of devices with a lateral structure for quantifying disorder, the technique was applied to the lateral structures of five different organic solar cell blends (PBDB-T:ITIC, PM6:O-IDTBR, PM6:Y6, PTB7-Th:COi8DFIC, and PTB7-Th:PC$_{71}$BM). Sensitive EQE$_{PV}$ spectra were measured for each device (shown in Figure S4, Supporting Information) and the technique was applied to extract the values depicted in Figure 6b. The results of Figure 2 and Figure S1 (Supporting Information) are also plotted here to make comparisons between σ_S values extracted using lateral structures and devices with inverted/conventional organic solar cell architectures. From this figure, it could be concluded that regardless of the uncertainty associated with the technique, it can be used to compare the energetic disorder associated with different blends. For example, the excitonic static disorder associated with COi8DFIC in a PTB7-Th:COi8DFIC active layer (102 meV) is more than twice the excitonic disorder associated with ITIC in a PBDB-T:ITIC active layer (42 meV). It could also be concluded that (even though devices with an inverted organic solar cell architecture are used), the average σ_S value for ITIC in both PBDB-T:ITIC and PM6:ITIC is roughly 39 meV. However, the accuracy of these values is questionable when, for example, the results obtained for the Y6 component of PM6:Y6 devices, using both a lateral structure and a
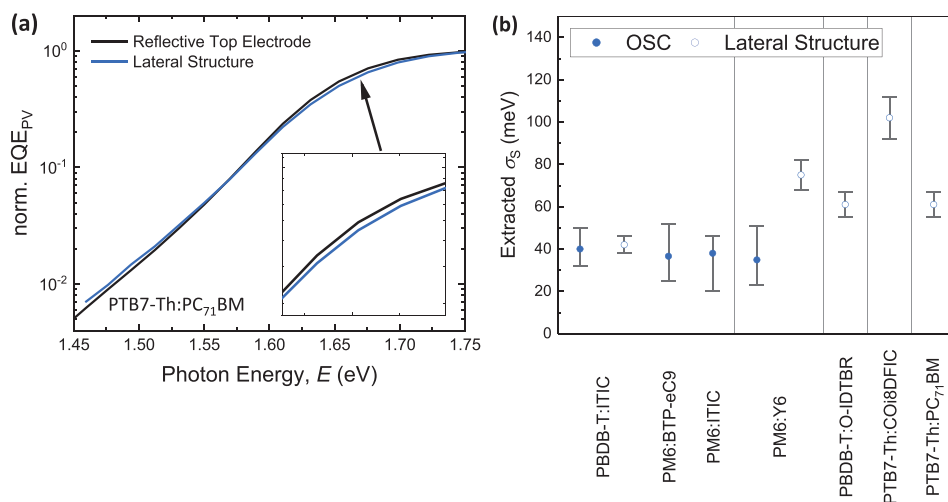

Figure 6. Experimental results of the investigation using devices with a lateral structure. a) A comparison between the EQE$_{PV}$ line-shapes of PTB7-Th:PC$_{71}$BM devices as a model system in devices with a (conventional) reflective top electrode architecture (black line) and a lateral structure (blue line). b) The excitonic static disorder values extracted for the narrower optical gap components of a variety of D-A blends, where results are compared for both organic solar cell (OSC) and lateral structure architectures. These values were obtained through the application of Equation (3) and (4) to the EQE$_{PV}$ spectra shown in Figure S4 (Supporting Information). For each blend, a mean value for the excitonic static disorder was computed (where applicable) from the values shown in Table S2 (Supporting Information). Here, the error bars associated with the lateral structure results indicate the ± 10% relative uncertainty attributed to each of the σ_S values, as per the results of the simulations. Whereas the error bars associated with the OSC results indicate the d_{AL}-dependent variations in σ_S around a mean value.

conventional organic solar cell architecture (with a reflective top electrode), are very different (with no overlap between the error bars). This suggests that either σ_S is quantified with great inaccuracy using devices with a conventional organic solar cell architecture, or that the PM6:Y6 lateral structure was more disordered than its organic solar cell counterpart, with the former case being more probable. Based on all the results of Figure 6, it could be concluded that the values for the excitonic static disorder determined using the technique described in this work are typically less than those extracted for neat films using wavelength-dependent internal quantum efficiency measurements.[37]

3. Conclusion

Through the application of a model for the SE absorption coefficient, $\alpha(E)$, we have presented a detailed methodology and an associated computational tool for the determination of the excitonic static disorder, σ_S, in organic semiconductors. This methodology can be applied to both neat films and blends, with the caveat that only the absorption of the narrower optical gap component of the latter can be parametrized. Utilizing an optical transfer-matrix model, we have also demonstrated the adverse effects of optical interference on the methodology. To overcome these limitations, we have presented two high-transparency device architectures. One of them (the lateral structure) was shown to be more ideal, owing to minimal optical interference, and the other (the cell with a transparent top electrode) was suggested to be the more practical architecture, provided that devices with thin active layers (less than 250 nm) are used. Following this, the lateral structure was used to quantify the energetic disorder associated with the narrower optical gap components of five systems-of-interest to the organic photovoltaic community.

The presence of thickness-dependent variations in the excitonic static disorder obtained from the simulated EQE_{PV} spectra of lateral structures indicate that there lies an inherent source of uncertainty in the methodology; this uncertainty is likely to arise from the pre-factor of Equation (4) having behavior that is dependent on the photon energy and the active layer thickness. Further work to minimize this uncertainty could include the development of a computational tool to numerically estimate the photon energy-dependent behavior of α_{sat} and EQE_0, in Equation (3) and (4), respectively. If such a tool were to work accurately, the line-shape of the EQE_{PV} could even be suitably adjusted in organic solar cells with reflective top electrodes, making the use of lateral structures and cells with transparent top electrodes redundant. However, as this tool would rely on the optical constants of all layers within the device, it could therefore be limited by the challenge of accurately determining the active layer's sub-gap extinction coefficient.

Using the methodology outlined in this work, alongside the MATLAB script that has been provided as supporting material, the static disorder can be quantified in several systems using room-temperature EQE_{PV} measurements. Then, by comparing the excitonic static disorder in these systems with important parameters such as the exciton lifetime, or figures-of-merit such as the fill factor or the non-radiative V_{OC} loss, any potential correlations between the two could be identified and investigated

further. Furthermore, the excitonic static disorder could be calculated and compared for organic semiconductors in both neat films and D:A blends. For example, σ_S could be determined and compared for neat ITIC, ITIC in PM6:ITIC, ITIC in PBDB-T:ITIC, and more to investigate what effect blending two organic semiconductors may have on the excitonic static disorder of the narrower optical gap component. Following this, the methodology could be applied to compare the energetic disorder associated with D:A blends in bi-layer and BHJ active layer morphologies. We believe this approach to be relatively straightforward in terms of experimental complexity, accurate, and generic for organic semiconductors and D:A blends.

4. Experimental Section

Materials: **BTP-eC9**: 2,2″-[[12,13-Bis(2-butyloctyl)-12,13-dihydro-3,9-dinonylbisthieno[2″‴,3″‴:4′,5′]thieno[2′,3′:4,5]pyrrolo[3,2-e:2″,3′-g][2,1,3]benzothiadiazole-2,10-diyl]bis[methylidyne(5,6-chloro-3-oxo-1H-indene-2,1(3H)-diylidene)]]bis[propanedinitrile]

CO*i*8DFIC: 2,2′-[[4,4,11,11-tetrakis(4-hexylphenyl)-4,11-dihydrothieno[2′, 3′:4,5]thieno[2,3-d]thieno[2″″,3″″:4″′,5″′]thieno[2″′,3″′:4″,5″]pyrano[2″,3′:4′,5′]thieno[2,3:4,5]thieno[3,2-b]pyran-2,9-diyl]bis[methylidyne(5,6-difluoro)]]

ITIC: 3,9-bis(2-methylene-(3-(1,1-dicyanomethylene)-indanone))-5,5,11,11-tetrakis(4-hexylphenyl)-dithieno[2,3-d:2′,3′-d′]-s-indaceno[1,2-b:5,6-b′]dithiophene

O-IDTBR: (5Z,5″Z)-5,5″-((7,7″-(4,4,9,9-tetraoctyl-4,9-dihydro-s-indaceno-[1,2-b:5,6-b″]dithiophene-2,7-diyl)bis(benzo[c][1,2,5]thiadiazole-7,4-diyl))bis(methanylylidene))bis(3-ethyl-2-thioxothiazolidin-4-one)

PBDB-T: Poly[(2,6-(4,8-bis(5-(2-ethylhexyl)thiophen-2-yl)-benzo[1,2-b:4,5-b′]dithiophene))-*alt*-(5,5-(1″,3″-di-2-thienyl-5′,7′-bis(2-ethylhexyl)benzo[1′,2′-c:4′,5′-c′]dithiophene-4,8-dione)]

PC₇₁BM: [6,6]-phenyl-C71-butyric acid methyl ester

PDINO:2,9-bis[3-(dimethyloxidoamino)propyl]anthra[2,1,9-def:6,5,10-d′e′f′]diisoquinoline-1,3,8,10(2H,9H)-tetrone

PEDOT:PSS: Poly(3,4-ethylenedioxythiophene) polystyrene sulfonate

PM6: Poly[(2,6-(4,8-bis(5-(2-ethylhexyl-3-fluoro)thiophen-2-yl)-benzo-[1,2-b:4,5-b′]dithiophene))-*alt*-(5,5-(1′,3′-di-2-thienyl-5′,7′-bis(2-ethylhexyl)benzo[1′,2′-c:4′,5′-c′]dithiophene-4,8-dione)]

PTB7-Th: Poly[4,8-bis(5-(2-ethylhexyl)thiophen-2-yl)benzo[1,2-b;4,5-b′]dithiophene-2,6-diyl-alt-(4-(2-ethylhexyl)-3-fluorothieno[3,4-b]thiophene-)-2-carboxylate-2-6-diyl)]

Y6: 2,2′-((2Z,2′Z)-((12,13-bis(2-ethylhexyl)-3,9-diundecyl-12,13-dihydro-[1,2,5]thiadiazolo[3,4-e]thieno[2″,3″:4′,5′]thieno[2′,3′:4,5]pyrrolo[3,2-g]thieno[2′,3′:4,5]thieno[3,2-b]indole-2,10-diyl)bis(methanylylidene))bis(5,6-difluoro-3-oxo-2,3-dihydro-1H-indene-2,1-diylidene))dimalononitrile

PC₇₁BM was purchased from Ossila (UK). O-IDTBR was purchased from Sigma-Aldrich (USA). CO*i*8DFIC, ITIC, PBDB-T, and PTB7-Th were purchased from Zhi-yan (Nanjing). BTP-eC9, PDINO, PM6, and Y6 were purchased from Solarmer (Beijing). PEDOT:PSS was purchased from Heraeus (Germany).

Device Fabrication: Substrate preparation: Commercially-patterned ITO coated glass and ultra-flat quartz-coated glass from Ossila were used for all devices in this work. All the substrates were sonicated in deionized water, acetone, and 2-propanol for 10 min each. The cleaned substrates were first dried by nitrogen and 110 °C hotplate and then treated in UV-Ozone cleaner (Ossila, L2002A2-UK) for 20 min.

Devices with an Inverted/Conventional Organic Solar Cell Architecture: The thicknesses of all the following films were determined using ellipsometry.

PBDB-T:ITIC and **PM6:ITIC** active layer thickness-dependent devices were fabricated with an inverted architecture (ITO/ZnO/Active Layer/MoO₃/Ag). The ZnO electron transport layer was prepared by dissolving 200 mg zinc acetate dihydrate in 2-methoxyethanol (2 mL) using ethanolamine (56 μL) as the stabilizer. The solution was stirred overnight

**ADVANCED
SCIENCE NEWS**

www.advancedsciencenews.com

**ADVANCED
FUNCTIONAL
MATERIALS**

www.afm-journal.de

under ambient conditions and spin-coated (4000 rpm for 30 s) onto the ITO substrates then annealed at 200 °C for 1 h to obtain a thickness of ≈30 nm. To fabricate devices with a PBDB-T:ITIC active layer, PBDB-T:ITIC with a D:A ratio of 1:1 was dissolved in a CB:DIO (99:1, v/v) solution to give various total concentrations. In addition, to fabricate devices with a PM6:ITIC active layer, PM6:ITIC with a D:A ratio of 1:1 was dissolved in a CF:DIO (99:1, v/v) solution to give various total concentrations. The exact concentrations and spin-coating speeds required to form the PBDB-T:ITIC and PM6:ITIC active layers (of varied thickness) considered in this work are given in Table S3 (Supporting Information). The as-cast films were then thermally annealed at 100 °C for 10 min. Following this, 10 nm of MoO_3 and 100 nm of Ag were deposited on the active layer to form a cathode.

PM6:BTP-eC9 and **PM6:Y6** active layer thickness-dependent devices were fabricated with a conventional architecture (ITO/PEDOT:PSS/ Active Layer/PDINO/Ag). The PEDOT: PSS solution was first diluted with the same volume of water, then cast at 4000 rpm onto the ITO substrate, followed by thermal annealing at 155 °C for 15 min to produce a 10 nm film. To fabricate devices with a PM6:BTP-eC9 active layer, PM6:BTP-eC9 with a D:A ratio of 1:1.2 by weight was dissolved in a CF:DIO (99.5:0.5) solution to give various total concentrations. In addition, to fabricate devices with a PM6:Y6 active layer, PM6:Y6 with a D:A ratio of 1:1.2 by weight was dissolved in a CF:CN (99.5:0.5) solution to give a variety of total concentrations. The exact concentrations and spin-coating speeds required to form the PM6:BTP-eC9 and PM6:Y6 active layers (of varied thickness) considered in this work are given in Table S4 (Supporting Information). The active layers were further thermally annealed at 100 °C for 10 min. Following this, a PDINO solution of concentration 1 mg mL^{-1} was spin-coated onto the active layers at 2000 rpm to form 10 nm films, and 100 nm of Ag was evaporated as to form the top electrode.

Devices with a Lateral Structure: Devices with a lateral structure were fabricated to avoid the optical interference effects that arise inside conventionally-structured OSCs. These devices were fabricated by spin-coating the active layer onto a pre-cleaned glass substrate before evaporating 100 nm Ag to form a cathode and an anode separated by a distance of 30 μm. The exact D:A ratios, solvents, concentrations, and spin-coating speeds used to fabricate the PBDB-T:ITIC, PBDB-T:O-IDTBR, PTB7-Th:COi8DFIC, PTB7-Th:PC$_{71}$BM, and PM6:Y6 lateral structures are given in Table S5 (Supporting Information).

Device Characterisation: Photovoltaic external quantum efficiency (EQE$_{PV}$): Sensitive photovoltaic external quantum efficiency (EQE$_{PV}$) measurements were conducted using a high-performance spectrophotometer (PerkinElmer, Lambda950) as a light source. The probe light beam was physically chopped at 273 Hz (Thorlabs, MC2000B) prior focusing on the device under test (DUT). The DUT photocurrent signal was measured by a lock-in amplifier (Stanford Research, SR860) in combination with a current pre-amplifier with an integrated, low-noise voltage source (FEMTO, DLCPA-200). For DUTs with conventional (lateral) device architecture, a bias voltage of 0 V (10 V) was applied. A detailed description of the EQE$_{PV}$ apparatus is provided elsewhere.[48]

Supporting Information

Supporting Information is available from the Wiley Online Library or from the author.

Acknowledgements

Conflict of Interest

The authors declare no conflict of interest.

Data Availability Statement

The data that support the findings of this study are available in the supplementary material of this article.

[1] H. Bässler, A. Köhler, in *Electronic Processes in Organic Semiconductors: An Introduction*, John Wiley & Sons **2015**. p. 1.

[2] J.-v. Vuuren, R. D. A. Armin, A. K. Pandey, P. L. Burn, P. Meredith, *Adv. Mater.* **2016**, *28*, 4766.

[3] A. Armin, W. Li, O. J. Sandberg, Z. Xiao, L. Ding, J. Nelson, D. Neher, K. Vandewal, S. Shoaee, T. Wang, H. Ade, T. Heumüller, C. Brabec, P. Meredith, *Adv. Energy Mater.* **2021**, *11*, 2003570.

[4] K. Fukuda, K. Yu, T. Someya, *Adv. Energy Mater.* **2020**, *10*, 2000765.

[5] L. Duan, A. Uddin, *Adv. Sci.* **2020**, *7*, 1903259.

[6] C. L. Cutting, M. Bag, D. Venkataraman, *J. Mater. Chem. C* **2016**, *4*, 10367.

[7] H. K. H. Lee, Z. Li, J. R. Durrant, W. C. Tsoi, *Appl. Phys. Lett.* **2016**, *108*, 253301.

[8] M. Mainville, M. Leclerc, *ACS Energy Lett.* **2020**, *5*, 1186.

[9] Y. Cai, Y. Li, R. Wang, H. Wu, Z. Chen, J. Zhang, Z. Ma, X. Hao, Y. Zhao, C. Zhang, F. Huang, Y. Sun, *Adv. Mater.* **2021**, *33*, 2101733.

[10] J. Song, L. Zhu, C. Li, J. Xu, H. Wu, X. Zhang, Y. Zhang, Z. Tang, F. Liu, Y. Sun, *Matter* **2021**, *4*, 2542.

[11] T. Kirchartz, K. Taretto, U. Rau, *J. Phys. Chem. C* **2009**, *113*, 17958.

[12] J. Jeong, M. Kim, J. Seo, H. Lu, P. Ahlawat, A. Mishra, Y. Yang, M. A. Hope, F. T. Eickemeyer, M. Kim, Y. J. Yoon, I. W. Choi, B. P. Darwich, S. J. Choi, Y. Jo, J. H. Lee, B. Walker, S. M. Zakeeruddin, L. Emsley, U. Rothlisberger, A. Hagfeldt, D. S. Kim, M. Grätzel, J. Y. Kim, *Nature* **2021**, *592*, 381.

[13] J.-Y. Kim, J. Yang, J. H. Yu, W. Baek, C.-H. Lee, H. J. Son, T. Hyeon, M. J. Ko, *ACS Nano* **2015**, *9*, 11286.

[14] J. Yang, J.-Y. Kim, J. H. Yu, T.-Y. Ahn, H. Lee, T.-S. Choi, Y.-W. Kim, J. Joo, M. J. Ko, T. Hyeon, *Phys. Chem. Chem. Phys.* **2013**, *15*, 20517.

[15] H. Bässler, A. Köhler, in *Electronic Processes in Organic Semiconductors: An Introduction*, John Wiley & Sons **2015**. p. 87.

[16] S. Athanasopoulos, E. V. Emelianova, A. B. Walker, D. Beljonne, *Phys. Rev. B* **2009**, *80*, 195209.

[17] M. Ansari-Rad, S. Athanasopoulos, *Phys. Rev. B* **2018**, *98*, 085204.

[18] O. V. Mikhnenko, P. W. M. Blom, T.-Q. Nguyen, *Energy Environ. Sci.* **2015**, *8*, 1867.

**ADVANCED
SCIENCE NEWS**

www.advancedsciencenews.com

**ADVANCED
FUNCTIONAL
MATERIALS**

www.afm-journal.de

[19] S. Athanasopoulos, H. Bässler, A. Köhler, *J. Phys. Chem. Lett.* **2019**, *10*, 7107.

[20] I. I. Fishchuk, A. Kadashchuk, S. T. Hoffmann, S. Athanasopoulos, J. Genoe, H. Bässler, A. Köhler, *Phys. Rev. B* **2013**, *88*, 125202.

[21] R. Coehoorn, P. A. Bobbert, *physica status solidi(a)* **2012**, *209*, 2354.

[22] S. Liu, J. Yuan, W. Deng, M. Luo, Y. Xie, Q. Liang, Y. Zou, Z. He, H. Wu, Y. Cao, *Nat. Photonics* **2020**, *14*, 300.

[23] T. Heumueller, T. M. Burke, W. R. Mateker, I. T. Sachs-Quintana, K. Vandewal, C. J. Brabec, M. D. McGehee, *Adv. Energy Mater.* **2015**, *5*, 1500111.

[24] J. C. Blakesley, D. Neher, *Phys. Rev. B* **2011**, *84*, 075210.

[25] S. N. Hood, I. Kassal, *J. Phys. Chem. Lett.* **2016**, *7*, 4495.

[26] N. Jain, N. Chandrasekaran, A. Sadhanala, R. H. Friend, C. R. McNeill, D. Kabra, *J. Mater. Chem. A* **2017**, *5*, 24749.

[27] Q. Guo, Y. Liu, M. Liu, H. Zhang, X. Qian, J. Yang, J. Wang, W. Xue, Q. Zhao, X. Xu, W. Ma, Z. Tang, Y. Li, Z. Bo, *Adv. Mater.* **2020**, *32*, 2003164.

[28] A. Classen, C. L. Chochos, L. Lüer, V. G. Gregoriou, J. Wortmann, A. Osvet, K. Forberich, I. McCulloch, T. Heumüller, C. J. Brabec, *Nat. Energy* **2020**, *5*, 711.

[29] O. J. Sandberg, A. Armin, *J. Phys. Chem. C* **2021**, *125*, 15590.

[30] F. D. Eisner, M. Azzouzi, Z. Fei, X. Hou, T. D. Anthopoulos, T. J. S. Dennis, M. Heeney, J. Nelson, *J. Am. Chem. Soc.* **2019**, *141*, 6362.

[31] C. Kaiser, O. J. Sandberg, N. Zarrabi, W. Li, P. Meredith, A. Armin, *Nat. Commun.* **2021**, *12*, 3988.

[32] I. Lange, J. C. Blakesley, J. Frisch, A. Vollmer, N. Koch, D. Neher, *Phys. Rev. Lett.* **2011**, *106*, 216402.

[33] A. Karki, G.-J. A. H. Wetzelaer, G. N. M. Reddy, V. Nádaždy, M. Seifrid, F. Schauer, G. C. Bazan, B. F. Chmelka, P. W. M. Blom, T.-Q. Nguyen, *Adv. Funct. Mater.* **2019**, *29*, 1901109.

[34] H. Bässler, *physica status solidi(b)* **1993**, *175*, 15.

[35] H. Bässler, A. Köhler, in *Unimolecular and Supramolecular Electronics I: Chemistry and Physics Meet at Metal-Molecule Interfaces* (Ed: R. M. Metzger), **2012**, Springer Berlin Heidelberg, Berlin, Heidelberg pp. 1–65.

[36] T. M. Burke, S. Sweetnam, K. Vandewal, M. D. McGehee, *Adv. Energy Mater.* **2015**, *5*, 1500123.

[37] S. Hood, N. Zarrabi, P. Meredith, I. Kassal, A. Armin, *J. Phys. Chem. Lett.* **2019**, *10*, 3863.

[38] N. A. Ran, J. A. Love, C. J. Takacs, A. Sadhanala, J. K. Beavers, S. D. Collins, Y. Huang, M. Wang, R. H. Friend, G. C. Bazan, T.-Q. Nguyen, *Adv. Mater.* **2016**, *28*, 1482.

[39] K. Vandewal, K. Tvingstedt, A. Gadisa, O. Inganäs, J. V. Manca, *Phys. Rev. B* **2010**, *81*, 125204.

[40] N. Zarrabi, O. J. Sandberg, S. Zeiske, W. Li, D. B. Riley, P. Meredith, A. Armin, *Nat. Commun.* **2020**, *11*, 5567.

[41] C. Kaiser, S. Zeiske, P. Meredith, A. Armin, *Adv. Opt. Mater.* **2020**, *8*, 1901542.

[42] A. Armin, N. Zarrabi, O. J. Sandberg, C. Kaiser, S. Zeiske, W. Li, P. Meredith, *Adv. Energy Mater.* **2020**, *10*, 2001828.

[43] F.-J. Kahle, A. Rudnick, H. Bässler, A. Köhler, *Mater. Horiz.* **2018**, *5*, 837.

[44] C. Göhler, M. Saladina, Y. Wang, D. Spoltore, J. Benduhn, K. Leo, C. Deibel, *Phys. Rev. Appl.* **2021**, *15*, 064009.

[45] J. Tang, *Chem. Phys.* **1994**, *188*, 143.

[46] J. Casado-Pascual, M. Morillo, I. Goychuk, P. Hänggi, *J. Chem. Phys.* **2003**, *118*, 291.

[47] T. H. Keil, *Phys. Rev.* **1966**, *144*, 582.

[48] S. Zeiske, C. Kaiser, P. Meredith, A. Armin, *ACS Photonics* **2020**, *7*, 256.

[49] A. Armin, I. Kassal, P. E. Shaw, M. Hambsch, M. Stolterfoht, D. M. Lyons, J. Li, Z. Shi, P. L. Burn, P. Meredith, *J. Am. Chem. Soc.* **2014**, *136*, 11465.

[50] L. A. A. Pettersson, L. S. Roman, O. Inganäs, *J. Appl. Phys.* **1999**, *86*, 487.

[51] G. F. Burkhard, E. T. Hoke, M. D. McGehee, *Adv. Mater.* **2010**, *22*, 3293.

[52] D. J. Griffiths, in *Introduction to Electrodynamics (Fourth Edition)*, Pearson **2021**.